DRAFT

ORNL/sub/87-SA946/07

Properties and Performance of Ceramic Composite Components

DRAFT

November 29, 2000

Report Prepared by
R. H. Carter, S. W. Case, and K. L. Reifsnider
Department of Engineering Science and Mechanics
Virginia Polytechnic Institute and State University
Blacksburg, VA 24061

under
Subcontract Number 19X-SA496C

for

OAK RIDGE NATIONAL LABORATORY
Oak Ridge, Tennessee 37831

for the
U. S. DEPARTMENT OF ENERGY
under contract DE-AC05-96OR22464

TABLE OF CONTENTS

1. INTRODUCTION 2

2. PERFORMANCE OF NEXTEL/SIC COMPOSITE TUBES 3

2.1 FABRICATION 3
2.2 AXIAL TESTS 5
2.3 INTERNAL PRESSURE TESTS 13

3. ANALYSIS OF DATA 17

3.1 ELASTICITY OR "FORWARD" SOLUTION 17
3.2 NONLINEAR REGRESSION ANALYSIS OR "INVERSE" SOLUTION 19

4. EFFECT OF RANDOMLY DISTRIBUTED FIBERS ON THE TOUGHNESS OF FIBRIL-REINFORCED COMPOSITE MATERIALS 23

4.1 INTRODUCTION 23
4.2 CRACK CLOSURE PRESSURE FOR AN INCLINED FIBER 23
4.3 EXTENSION TO RANDOMLY DISTRIBUTED FIBERS 25
4.3.1 No Possible Fiber Pull-Out 25
4.3.2 Possible Fiber Pull-Out 28
4.4 CRACK OPENING AND STRESS INTENSITY FACTOR 28
4.5 NUMERICAL PROCEDURE 29

5. REFERENCES 33

1. Introduction[†]

The objective of the Fossil Energy Advanced Research and Technology Development (AR&TD) Materials program is to conduct research and development on materials for longer-term fossil energy applications as well as for generic needs of various fossil fuel technologies. These needs have prompted research aimed toward a better understanding of material behavior in fossil energy environments and the development of new materials capable of substantial enhancement of plant operations, reliability, and efficiency.

The research program of the Materials Response Group at Virginia Tech addresses the need for reliable and durable ceramic composites to perform in high temperature applications. Areas of current research are characterization of oxide/oxide hot gas filter tubes and dense Nextel/SiC tubes. The focus of this report will be on the characterization of the Nextel/SiC tubes. In Section 2, we discuss the tube responses to axial tensile and compression loading as well as to torsional loading. Internal pressure test procedures are detailed and refinements are proposed. In Section 3, the elasticity theory model and nonlinear regression analysis currently being developed will be explained and preliminary results presented.

Finally, we have been working toward the goal of developing models for the strength and toughness of fibril-reinforced composites. The first step toward this goal, described in the last report and summarized in Section 3, is to develop models for the bridging stresses in cases in which the bridging fibers are randomly oriented. This model has been extended to include the effect of fiber length, and is used to determine the apparent toughness of a fibril reinforced composite.

[†] Research sponsored by the U. S. Department of Energy, Fossil Energy Advanced Research and Technology Development Materials Program, DOE/FE AA 15 10 10 0, Work Breakdown Structure Element VPI-1

2. Performance of Nextel/SiC Composite Tubes

Much of the previous mechanical testing of composites made using the FCVI technique has been limited to relatively small planar samples. These test methods include flexure tests and some limited axial testing[3-6]. With the larger sample size and different sample geometry, different tests need to be performed to characterize the mechanical properties of tubular samples. The approach used in this study will be modeled after that applied in Carter, *et al* for characterizing hot gas filter tubes[1,8]. Axial tension, compression and torsion are used to characterize the elastic response of the tubes. Internal pressure and axial tensile strength tests are used to characterize the strength of the composite.

2.1 Fabrication

The composite tubes were fabricated using the forced-flow, thermal gradient chemical vapor infiltration technique at developed at Oak Ridge[2]. The preforms consisted of ten to twelve Nextel 610 (Nextel 312 for sample CVI-1173) braided sleeves stretched over a polyethylene mandrel. The green preform was infiltrated with a small amount of Borden Durite resin to provide some structural support prior to the silicon carbide infiltration. The preform was compressed by aluminum tube sections and allowed to cure. The cured preform was trimmed to a 35.5-cm length prior to the SiC infiltration via the FCVI process. The FCVI process conditions were as follow: 1200°C, 5 slm of hydrogen, and 1 slm of methyltrichlorosilane (MTS). The samples achieved 80 to 90% of theoretical densities in about 36 hours. Once processing was completed the ends of the samples were removed to leave a 30-cm long sample. The final tube properties are listed in Table I. It should be noted that in this study, no fugitive carbon layer was deliberately deposited to improve composite toughness. A small amount may be present from the decomposition of the resin used to rigidize the preform, though none was noticed in the initial inspection of the tubes.

Table I. Properties of the Nextel/SiC composite tubes

	CVI 1173	CVI 1216	CVI 1219
Process Time(hours)	36	36	36
Density (g/cm^2)	3.00	2.88	3.08
% Theoretical Density	87	~80	~80
Fiber Type	Nextel 312	Nextel 610	Nextel 610
Fiber Volume Fraction (%)	50	37.5	32.2
Number of layers	10	10	8

A cross section of the CVI-1173 tube can be seen in Figure 2-1. The light gray layer on the inner surface is a SiC layer deposited during the FCVI process. This layer was less than 1 mm at the ends of the tube, and approached 4 mm in thickness in some

cross sections taken near the middle of the sample. The uneven distribution of the SiC increases the difficulty in the calculation of the density. It is estimated to be near 80% theoretical

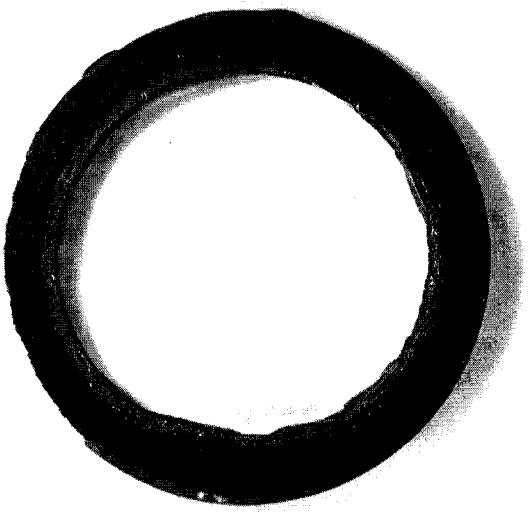

Figure 2-1: Cross section of sample 1173

density of the composite. Additionally, the change in dimension creates problems in accurately calculating the stress in the material. The cross sectional area and polar moment of inertia used in this study were calculated from the average values of the outer diameter and tube thickness at each end of the sample.

For Sample CVI 1219, the SiC layer was on the order of 4-mm thick, increasing the cross-sectional area, thereby decreasing the stress in the material during testing. Due to this, the strength of the sample exceeded the load capacity of the MTS system (246 kN). The steel inserts were removed by burning off the epoxy layer by placing the sample in a furnace at 400°C for 1 hour. The power was turned off and the system was allowed to cool before the sample was removed. The sample was returned to ORNL, and the SiC layer was machined off the inner surface. The average dimensions for the samples are in Table II. The changes in the dimensions of CVI 1219 are shown in the last two columns. The thickness values for the sample after milling exhibits large variations, which is due to the inner surface not being concentric with the outer.

Table II. Dimensions of the samples

In mm	**CVI 1173-1**	**CVI 1173-2**	**CVI 1216**	**CVI 1219** (as-received)	**CVI 1219** (after milling)
Outer Diameter	59.7±0.2	59.7±0.2	59.3±0.06	59.2±0.1	59.1±0.2
Thickness	6.9±0.7	6.8±0.4	7.6±0.6	7.9±1.8	4.8±0.4
Inner Diameter	45.8	46.1	43.9	43.4	49.7
Area ($*10^{-4}$ m^2)	11.48	11.24	13.09	14.99	8.14

2.2 *Axial tests*

Axial tension, torsion and compression tests were performed on each of the samples. All tests were performed on a MTS servo-hydraulic load frame with axial and torsional capabilities. Teststar II software from MTS handled system control and data acquisition. To increase the number of samples, CVI 1173 was cut in half. The later samples, CVI 1216 and 1219, were sectioned differently. From each of the tubes, two 3.5 to 4.0-cm internal pressure test samples were cut from the initial sample, leaving a 23-cm sample for axial testing. For the axial samples, the ends were initially potted in epoxy and machined down to acceptable tolerance for the MTS grips. The low stiffness of the epoxy proved insufficient to support the high compressive force in the grips. Both of the 1173 axial samples suffered grip-induced failures. To provide support, 6.25-cm long steel inserts were made to closely fit into the tube ends and were bonded in place with epoxy. Again, the outer surface was built up with epoxy and milled down to the tolerances required for the MTS grips. Grip related failures have not been observed on either sample using this configuration.

Strain measurements were made using four strain gage rosettes equally spaced around the samples as shown in Figure 2-2. The redundant measurements are made to account for any specimen misalignment, since small misalignments can generate significant stress/strain variations through the sample[8]. In the elastic regime (below matrix cracking), these effects can be removed by averaging the values. A typical axial stress/strain curve is located in Figure 2-3. The plotted values are the average of the different strain components from each gage. The recording of the different strain components (axial, hoop, and shear) is important for the analysis being developed and is explained in Section 3. Table III contains the measured mechanical properties of the tubes. Both sets of results are listed for Sample CVI 1219 – AR for as-received and AM for after-milling. The tensile strength values for the two 1173 samples are not indicative of the material since both exhibited grip induced failures.

Table III: Mechanical Properties of the Nextel/SiC composite tubes

Tube ID	Axial Stiffness (GPa)	Torsional Stiffness (GPa)	Poisson Ratio	Tensile Strength (MPa)
1173-1	171.6	91.3		31.1
1173-2	166.9	66.0		68.1
1216	163.8	80.6	0.28	>197.4 Axial + 43.5 Shear
1219 AR	141.5	64.7		>137
1219 AM	148.8	67.3	0.52	200.2

The stiffness values are calculated from the strain data collected from the strain gages and the stress values calculated using the values for the area and moment of inertia. It is uncertain why there is a large discrepancy in the torsional stiffness values between the two 1173 samples. Both samples were cut from the same tube, and the axial stiffness values are similar, indicating that there are no major differences in the geometry or material properties.

The stress/strain curves for the tensile strength tests of the CVI 1173 samples are in Figure 2-4. Both 1173 samples experienced grip induced failure, and exhibited a small amount of nonlinear behavior, as can be seen in the departure from the CVI 1216 line. The fracture surface exhibited some fiber pullout, as can be seen in Figure 2-10. CVI 1219 failed in the gage section, and the tensile strength plot is in Figure 2-5. An extension of the linear behavior of the material is included to illustrate the nonlinear behavior.

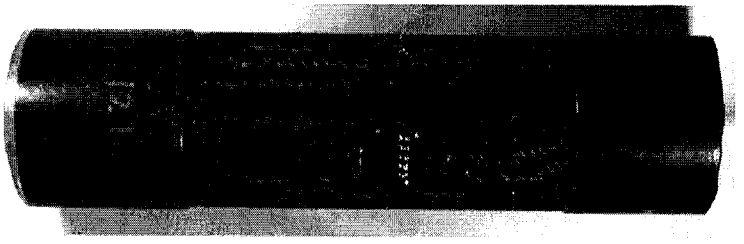

Figure 2-2: Specimen configuration for axial tube testing.

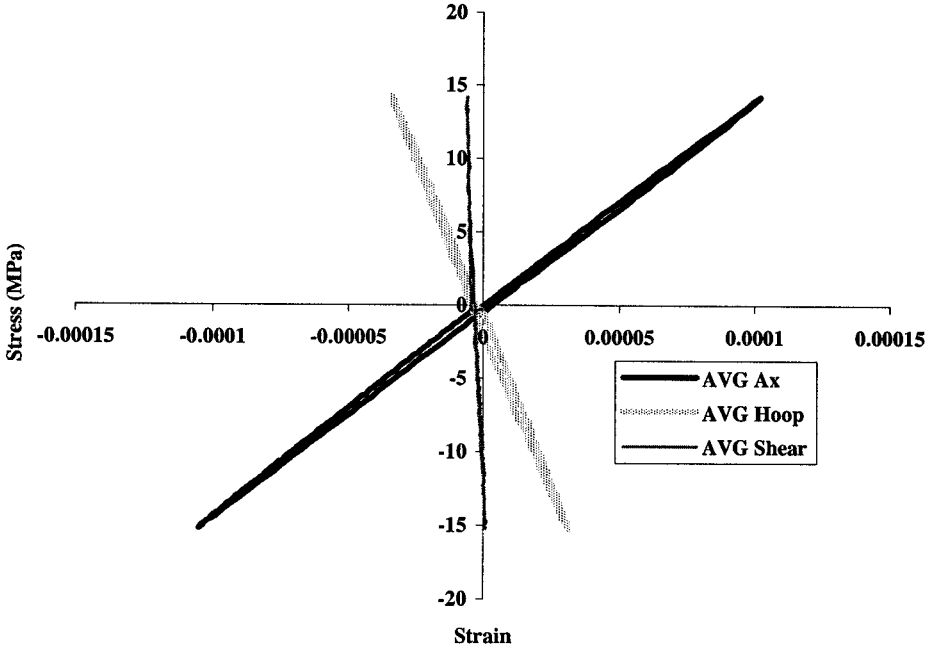

Figure 2-3: Typical tensile test.

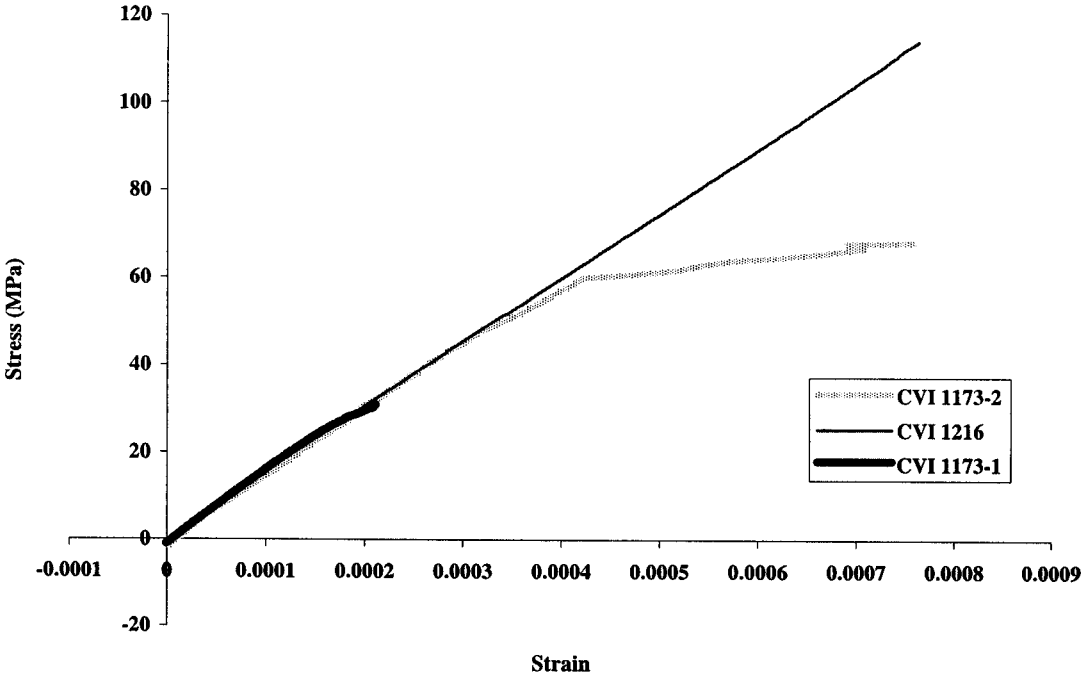

Figure 2-4: Stress/ Axial Strain curves for tensile strength tests

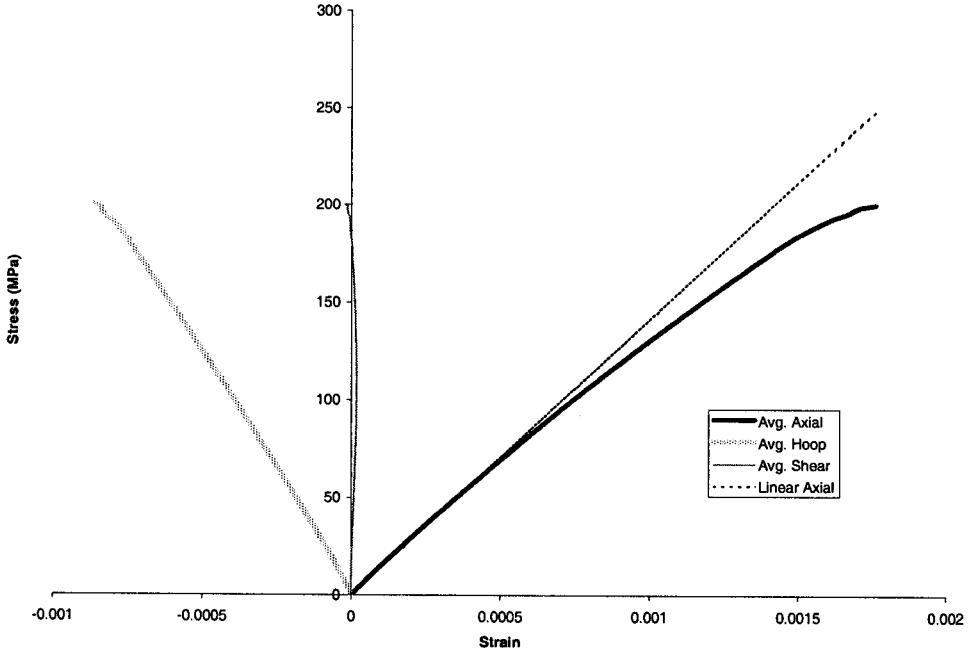

Figure 2-5. Tensile Strength Plot for CVI 1219.

During the testing of samples 1216 and 1219 AR, the load profile reached the system limit before failure. The values listed are the largest stress values applied before the 246kN (55 kip) limit or prior to slippage of the sample. In order to test CVI 1216 and 1219, the grip pressure was boosted to 38 MPa, from the normal setting of 20 MPa, to prevent slipping at the higher loads. For CVI 1216, the load profile was altered so that torque would be applied when the axial load limit was reached. The load profile for CVI 1216 is in Figure 2-6. The axial force reaches 246 kN and an applied torque of 1422 N-m before the sample slipped out of the grips of the MTS frame. Later attempts to repeat the test to a higher level failed due to wear on the epoxy grip surface.

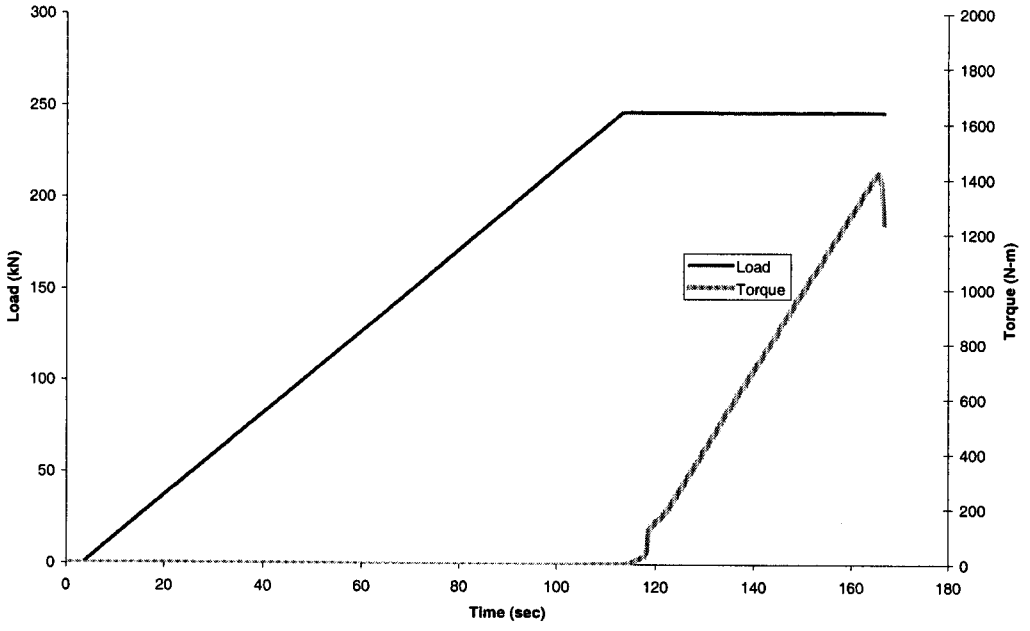

Figure 2-6. Load Profile for CVI 1216

Figure 2-7 and Figure 2-8 are of the strain response to the different sections of the loading profile. Figure 2-7 has the pure tension results, while 2-8 contains the result for the torque ramp with a constant 246 kN axial load.

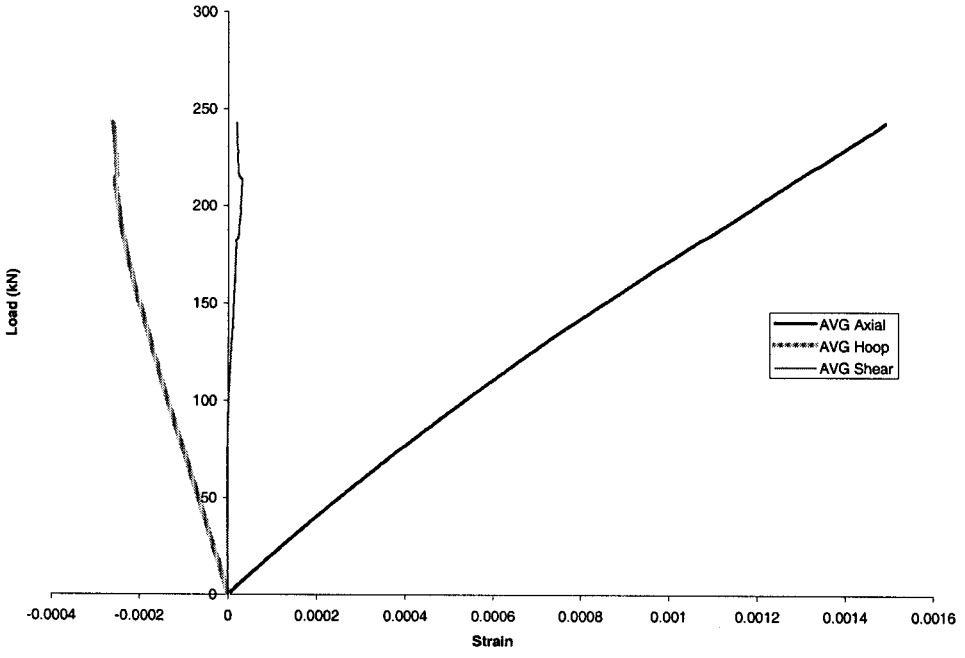

Figure 2-7. Strain response for the tension only portion of Figure 2-6

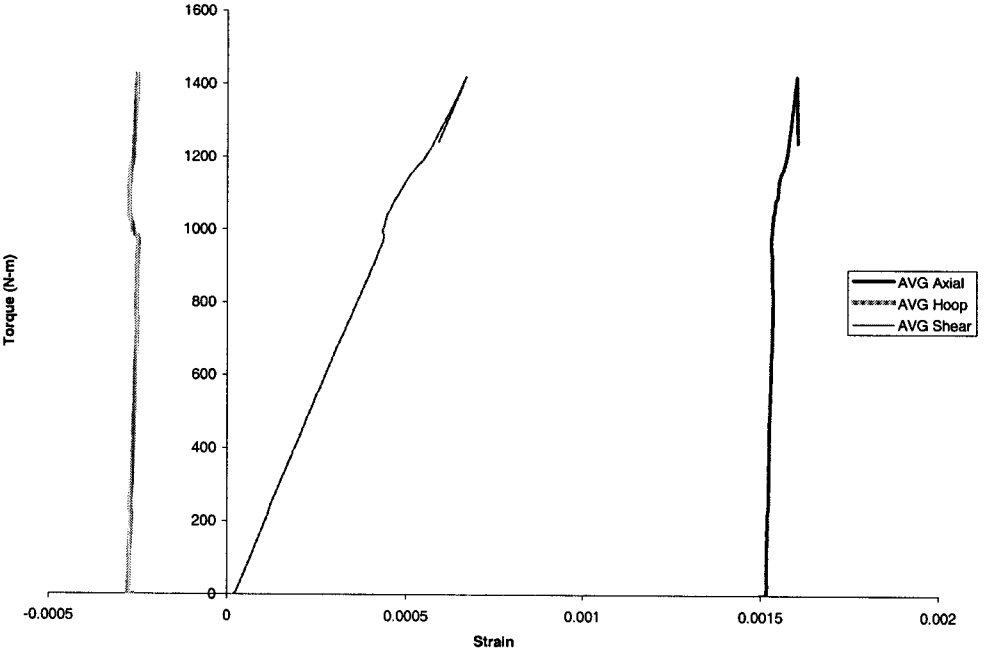

Figure 2-8. Strain response for the torque ramp with 246kN load

Photographs of the failed of samples CVI 1173, 1 and 2, and CVI 1219 are in Figure 2-9 through Figure 2-12. The first two images show the grip-induced failure of the CVI 1173-1. The failure originated in the region above the grip area, as can be seen in Figure 2-9. Figure 2-11 and Figure 2-12 are of CVI 1219. All the samples exhibited fiber pullout, while CVI 1219 had delamination and pullout (highlighted in Figure 2-11).

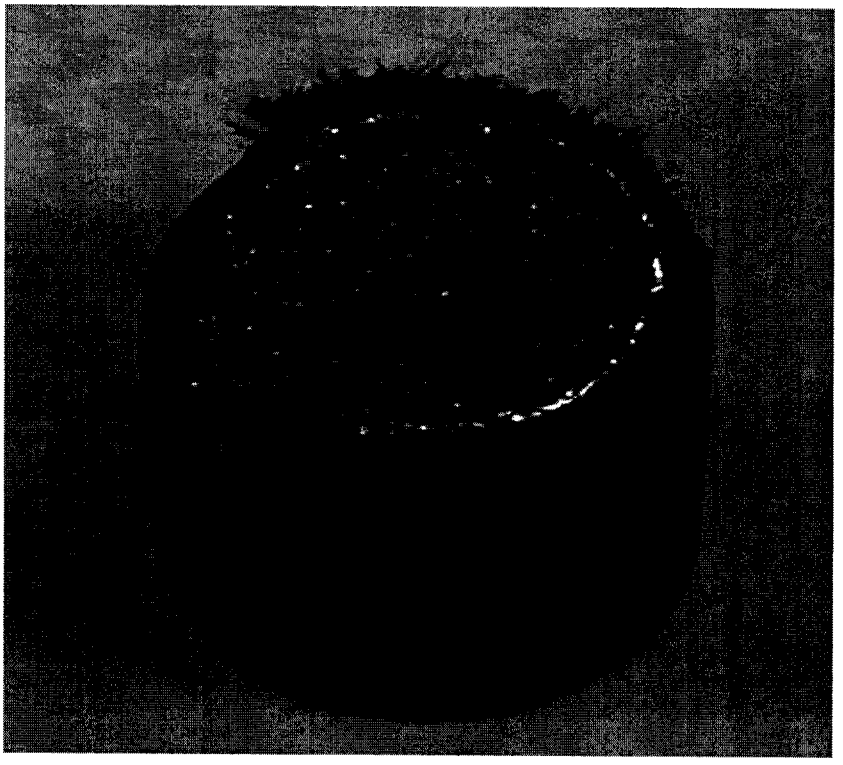

Figure 2-9. Grip induced failure of CVI 1173-1

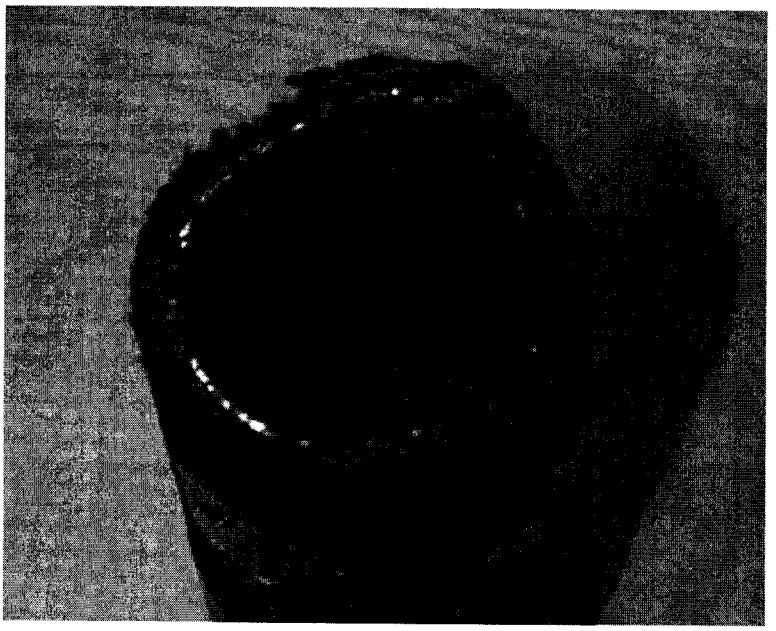

Figure 2-10: Fractured tensile strength specimen CVI 1173-1

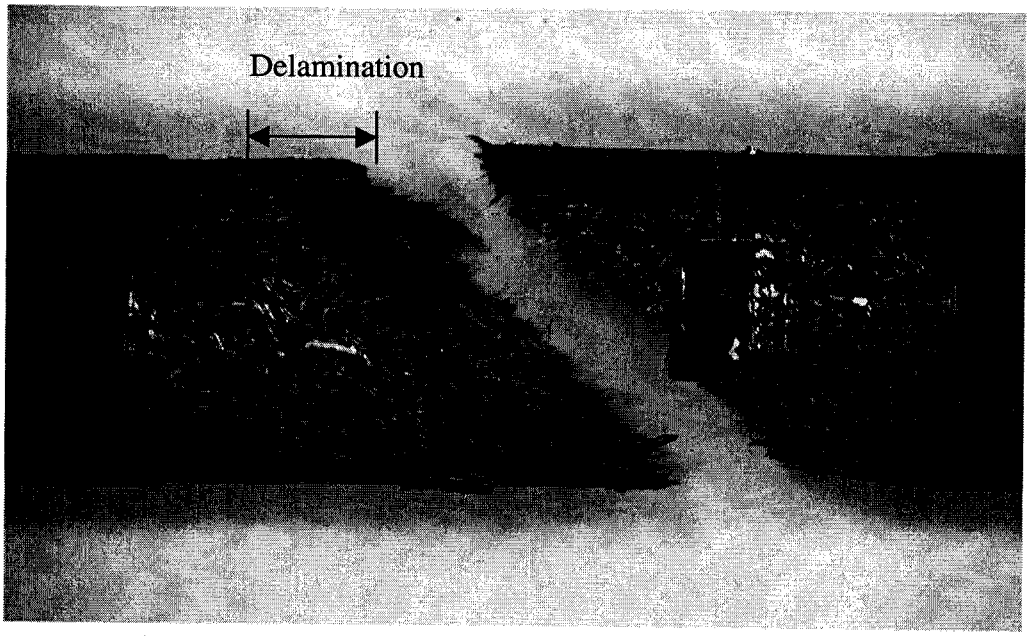

Figure 2-11. Sample CVI 1219 with large amounts of fiber pullout and delamination

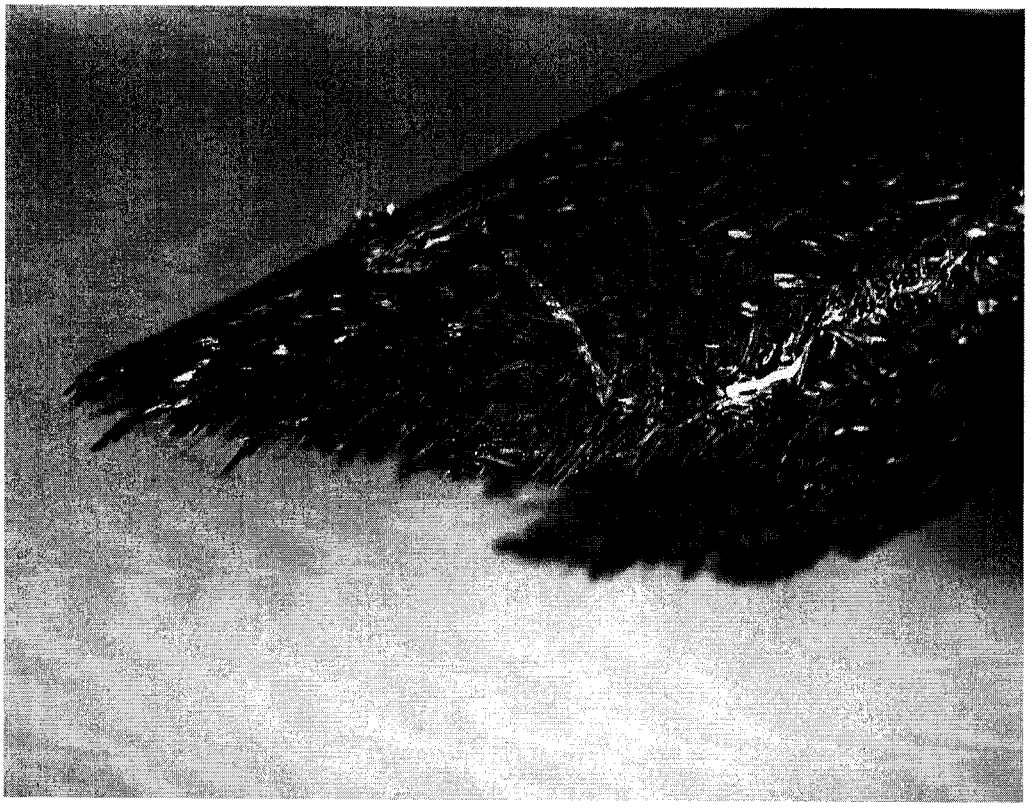

Figure 2-12. Sample CVI 1219 failure surface with pullout

2.3 *Internal pressure tests*

Internal pressure testing has been used for testing composite tubes[6-9]. The procedure used the compressed rubber plug technique as described in Singh, *et al.* A schematic of the test is in Figure 2-13. By compressing the rubber plug, the Poisson

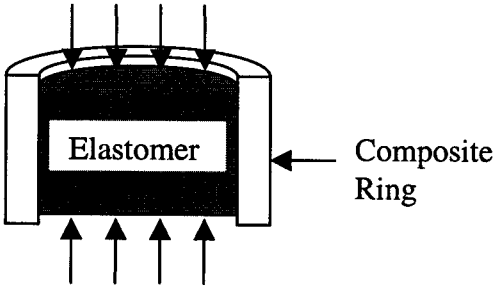

Figure 2-13: Schematic of internal pressure test

expansion of the material will generate pressure on the inner surface. The internal pressure is calculated by the expression:

$$P_i = \frac{\sigma_p - E_p \varepsilon_z}{2\nu_p} \tag{2.1}$$

Where P_i is the internal pressure, σ_p, E_p, ε_z and ν_p are the compressive stress, Young's modulus, axial strain, and Poisson's ratio for the plug material. This expression is derived from an elasticity solution for an isotropic, linear elastic material. Due to the axisymmetric loading conditions, the radial and hoop stress are equal throughout the plug[10]. With this information, Hooke's Law can be rearranged into the expression above. It is important to note that due to the large deformations used for these tests (30 to 50% on average), true stress and strain values should be used for this procedure. These values are found from the engineering stress and strain values by:

$$\begin{aligned} \tilde{\varepsilon} &= \ln(1+\varepsilon) \\ \tilde{\sigma} &= \sigma(1+\varepsilon) \end{aligned} \tag{2.2}$$

where $\tilde{\sigma}$ and $\tilde{\varepsilon}$ are the true stress and strain and σ and ε are the engineering stress and strain[11]. Initial attempts used a Dow Silastic T-2 silicon rubber plug. This material proved to be too soft for use with the SiC samples. At high pressures the plug would fail prior to failure of the specimen. The material was changed and a urethane rubber was used to generate pressure within the sample. The material has proved to be nonlinear elastic in compression, causing the equation above not to accurately predict the pressure. By changing the Young's modulus for the plug from a constant to a function of strain, the equation can describe the behavior of nonlinear elastic materials. To record this behavior, a plug is compressed between to lubricated platens using the same loading rate as for the internal pressure tests, and the data is fit using a polynomial expression (usually 5^{th} or 6^{th} order regression) in a Microsoft Excel spreadsheet. Each test is preformed with

the same loading rate and at least 10 minutes between tests, to minimize differences due to the visco-elastic effects of the elastomer compound. A high pressure lubricant is applied to both the plug and inner surface of the sample to minimize compressive loads generated by friction. After each test, the plug and sample are inspected for any damage associated with the test. To date, the tests have not been run to a level sufficient to damage the SiC composite. New elastomeric compounds are being investigated, and the procedures are being improved in the hope of increasing the pressure above the strength of the material.

Typical internal pressure test results are in Figure 2-14 and Figure 2-15. Figure 2-14 has the stress-strain curve of the plug within the sample (Constrained Plug Stress) and that of the compression of an unconstrained plug (Free Plug Stress).

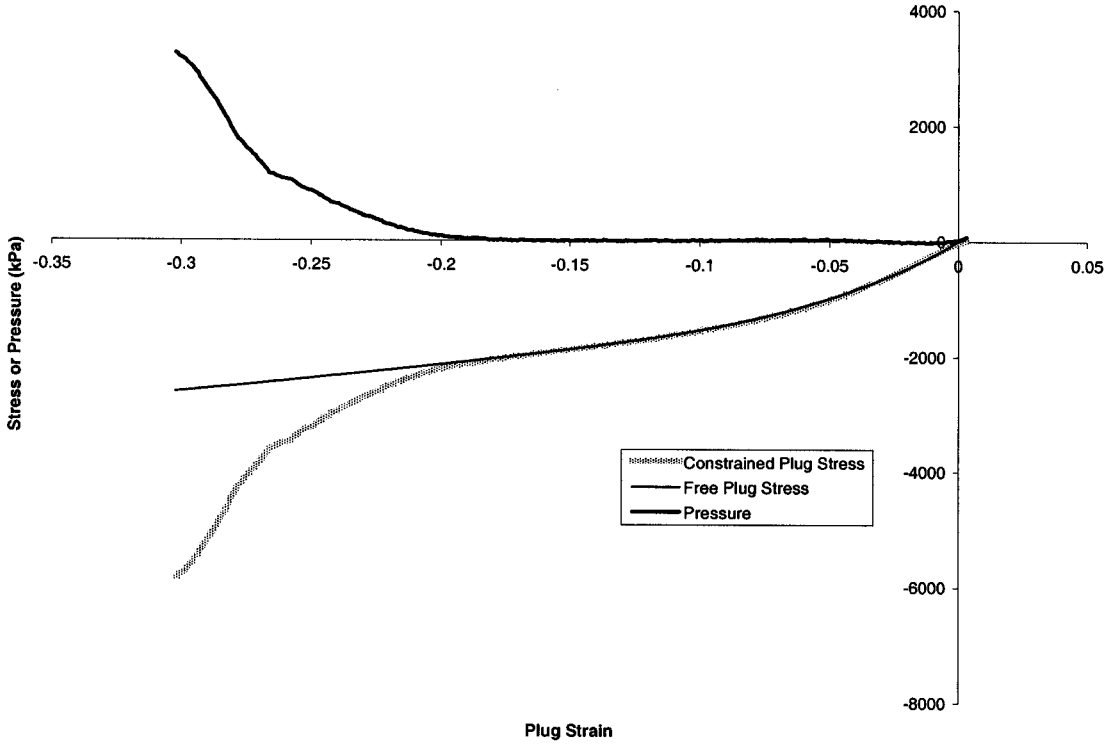

Figure 2-14. Stress and strain in the plug for an internal pressure test with the internal pressure generated in the sample.

The two curves overlap until the plug comes into contact with the inner surface of the sample at a value of –20% strain. From 20 to 30% strain the Constrained Plug stress differs from the Free Plug by the effects of the pressure generated. Figure 2-15 is a plot of the strain measured by the stain gages on the composite sample as a function of the internal pressure. The values below 1 MPa should be overlooked since it believed that below this value the plug has not made uniform contact with the surface of the sample. If the plug is not perfectly centered, the first part of test will be the plug making uneven

contact with the sample and centering due to unbalanced forces and lubricated surfaces. Also, for the axial measurements, the sample is held in a fixture with a compressive load to prevent sample movement. After the 1 MPa limit, the strains resume a linear trend with the application of pressure.

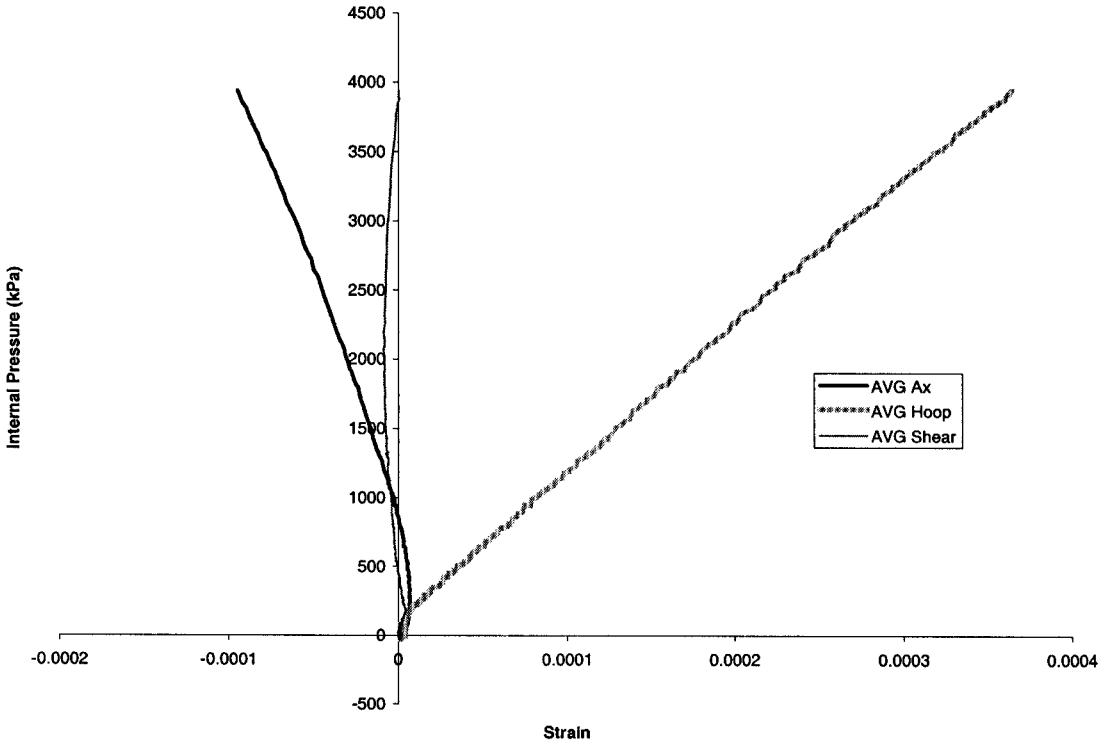

Figure 2-15. Measured strain vs. internal pressure for an internal pressure test (Sample CVI 1219).

The results of the internal pressure tests are in Table IV. The values are the slopes found by linear regression for the data, as shown in Figure 2-15 (Pressure/strain). Others in the literature have calculated the hoop stress in the cylinder due to the internal pressure by expressions from elasticity theory (Lame's Cylinder solution)[9]. This assumes a homogenous, isotropic material behavior, which is not expected with these materials, but will be used here to describe the results. It allows for the different thickness of the samples to be taken into consideration, which are significant between the 1216 and 1219 samples. Work described in the next section is being developed to address the problem of finding a better method to represent the results to internal pressure tests, since these materials are neither homogenous nor isotropic.

More work is needed to develop this procedure to a level where it will be able to differentiate between material properties and testing conditions. The differences in the Poisson ratio could be due to structural differences in the material or the difference in the surface finish of the inner surface. The inner surface of CVI 1219 was machined to a smooth surface, while CVI 1216 is uneven with large protrusions deposited during the

infiltration. Even with the lubrication, it would be enough to generate compressive loads in the sample, increasing the Poisson's ratio.

Table IV. Slopes of the best-fit data

	Pressure/Strain			Hoop Stress/Strain	
Sample	**Axial (GPa)**	**Hoop (Gpa)**	**Hoop (GPa)**	**Shear (GPa)**	**Poisson's ratio**
CVI 1216	-89.16	40.57	394.1	95.13	0.46
CVI 1219	-34.18	10.74	276.2	55.13	0.31

3. Analysis of Data

So far, the characterization of the composite tubes has focused on the global responses (axial stiffness and strength, torsional stiffness, and internal pressure burst tests). A better understanding of the material would come from knowing the ply-level elastic properties, but it is not possible to measure those directly for a composite tube. Current research is developing methods to determine the ply-level elastic constants (E_1, E_2, E_3, etc...) for a homogenous, orthotropic composite laminate. The first part of this section will review the elasticity solution for these structures subjected to axisymmetric loading conditions. In the second part, a nonlinear regression analysis will be detailed with some preliminary results.

3.1 Elasticity or "Forward" Solution

The derivation illustrated is from the work by Rousseau, *et al*[12]. The following expressions can be used to calculate the stresses, strains and displacements for a composite cylinder under axisymmetric loading conditions (axial tension, compression, torsion, internal pressure and uniform temperature change). By applying the Strain-Displacement relations to the Displacement equations, the different strain components can be calculated through the thickness of the tube. The strain values are related to the stress values by the Constitutive equations.

Displacement Equations – u = axial displacement, v = tangential and w = radial displacement

$$
\begin{aligned}
u(x) &= \varepsilon^o x \\
v(x,r) &= \gamma^o x r \\
w(r) &= A_1 r^{\lambda} + A_2 r^{-\lambda} + \Gamma \varepsilon^o r + \Omega \gamma^o r^2 + \Psi r \Delta T \\
\lambda &= \sqrt{\frac{\bar{C}_{22}}{\bar{C}_{33}}} \\
\Gamma &= \left(\frac{\bar{C}_{12} - \bar{C}_{13}}{\bar{C}_{33} - \bar{C}_{22}} \right) \\
\Omega &= \left(\frac{\bar{C}_{26} - 3\bar{C}_{36}}{4\bar{C}_{33} - \bar{C}_{22}} \right) \\
\Psi &= \left(\frac{(\bar{C}_{i2} - \bar{C}_{i3})\alpha_i}{\bar{C}_{33} - \bar{C}_{22}} \right)
\end{aligned}
\tag{3.1}
$$

Strain-Displacement Equations

$$\begin{aligned} \varepsilon_x &= \frac{\partial u}{\partial x} & \gamma_{r\theta} &= \frac{\partial v}{\partial r} - \frac{v}{r} \\ \varepsilon_\theta &= \frac{w}{r} & \gamma_{xr} &= \frac{\partial u}{\partial r} = 0 \\ \varepsilon_r &= \frac{\partial w}{\partial r} & \gamma_{x\theta} &= \frac{\partial x}{\partial \theta} = 0 \end{aligned} \tag{3.2}$$

Constitutive Equations

$$\begin{bmatrix} \sigma_x \\ \sigma_\theta \\ \sigma_r \\ \gamma_{\theta r} \\ \gamma_{xr} \\ \gamma_{x\theta} \end{bmatrix} = \begin{bmatrix} \overline{C}_{11} & \overline{C}_{12} & \overline{C}_{13} & 0 & 0 & \overline{C}_{16} \\ \overline{C}_{12} & \overline{C}_{22} & \overline{C}_{23} & 0 & 0 & \overline{C}_{26} \\ \overline{C}_{13} & \overline{C}_{23} & \overline{C}_{33} & 0 & 0 & \overline{C}_{36} \\ 0 & 0 & 0 & \overline{C}_{44} & \overline{C}_{45} & 0 \\ 0 & 0 & 0 & \overline{C}_{45} & \overline{C}_{55} & 0 \\ \overline{C}_{16} & \overline{C}_{26} & \overline{C}_{36} & 0 & 0 & \overline{C}_{66} \end{bmatrix} \begin{bmatrix} \varepsilon_x \\ \varepsilon_\theta \\ \varepsilon_r \\ \gamma_{\theta r} \\ \gamma_{xr} \\ \gamma_{x\theta} \end{bmatrix} \tag{3.3}$$

At this point the expressions for stress, strain and displacement can be derived in terms of the transformed material stiffness matrix ($\overline{C}_{ij}$), ε^0, γ^0, A_1 and A_2. Since the elastic properties and geometric considerations are known for a given structure, the $\overline{C}_{ij}$ values can be calculated for each ply. The remaining unknown terms - ε^0, γ^0, A_1 and A_2 – need to be found using the boundary conditions. For a laminated structure composed of N layers, there will be 2N+2 unknowns – ε^0, γ^0, N A_1's, and N A_2's. The first boundary condition is a relation between the applied axial force and the axial stress. For a tube in axial tension, the applied axial force, F_x, must be equal to the sum of the integrals of the axial stress through the thickness. The same applies to a tube with an applied torque, T_x. The sum of the integrals of the shear stress must equal the applied torque. The expressions for these boundary conditions are:

$$\begin{aligned} F_x &= 2\pi \sum_{k=1}^{N} \int_{r_{k-1}}^{r_k} \sigma_x^{(k)}(r) r dr \\ T_x &= 2\pi \sum_{k=1}^{N} \int_{r_{k-1}}^{r_k} \tau_{x\theta}^{(k)}(r) r^2 dr \end{aligned} \tag{3.4}$$

This gives two equations towards the 2N+2 unknowns. Two more come from the pressurized cylinder condition. The pressure at the inner and outer surfaces must be equal and opposite to the applied pressures. These can be equated as:

$$-p_i = \sigma_r^1(R_i)$$
$$-p_o = \sigma_r^N(R_o) \tag{3.5}$$

where p_i and p_o are in the applied internal and external pressures, R_i and R_o are the inner and outer radii, and the superscript on the stress expression is the layer of the material. The last two requirements for the tube are that of continuity of traction and displacements at ply interfaces, or:

$$w^{(k)}(r_k) = w^{(k+1)}(r_k)$$
$$\sigma_r^{(k)}(r_k) = \sigma_r^{(k+1)}(r_k) \tag{3.6}$$

This gives the last 2(N-1) equations needed to solve for the unknowns. Simultaneously solving the above equations will give the 2N+2 unknowns for the displacement, strain and stress equations.

3.2 Nonlinear Regression Analysis or "Inverse" Solution

Now that an analytic expression exists, it is possible to develop a method using this model to back calculate the ply level properties. In a thesis by George, a nonlinear regression method was used to find the best ply level elastic properties to fit a set of experimental data[13]. Figure 3-1 illustrates the steps in the nonlinear regression analysis. In the first step, the sample geometry (number of plies, orientation, interfacial radii, etc...), guess values for the elastic properties (E_1, E_2, E_3, G_{12}, ν_{12}, ν_{13}, ν_{23}, α_1, α_2 and α_3) and applied loads (F_x, T_x, P_i, P_o, and any combinations of each) are entered into the elasticity solution. The strain response (ε_x, ε_θ and $\gamma_{x\theta}$) for each load condition is calculated. At this point, there are two sets of strain values, the experimental data and those calculated from the guess values. The goal of the program is to minimize the error function, Y, which is defined as:

$$Y = \sum\sum\Phi^2 = \sum\sum(\varepsilon_m - \varepsilon_c)^2 \tag{3.7}$$

Where ε_m and ε_c are the measured and calculated strain values, and Y is the sum of square errors (SSE).

If the system of equations were linear, a minimum in the error function would be found in one step. Since this is not, a nonlinear regression technique must be used. The difference is that the nonlinear method is an iterative process, with each successive step decreasing the SSE. A solution is found by declaring convergence criteria. These can range from the SSE falling below a defined or acceptable value, or defining a fixed number of iterations for the system. Usually, more than one of the criteria will be employed to reduce computation time and determine convergence. Other criteria are chosen to stop the program if the system is not converging to a solution. This is dependent upon the quality of the data and guess values. If either is not sufficient, the system may not converge to a meaningful solution.

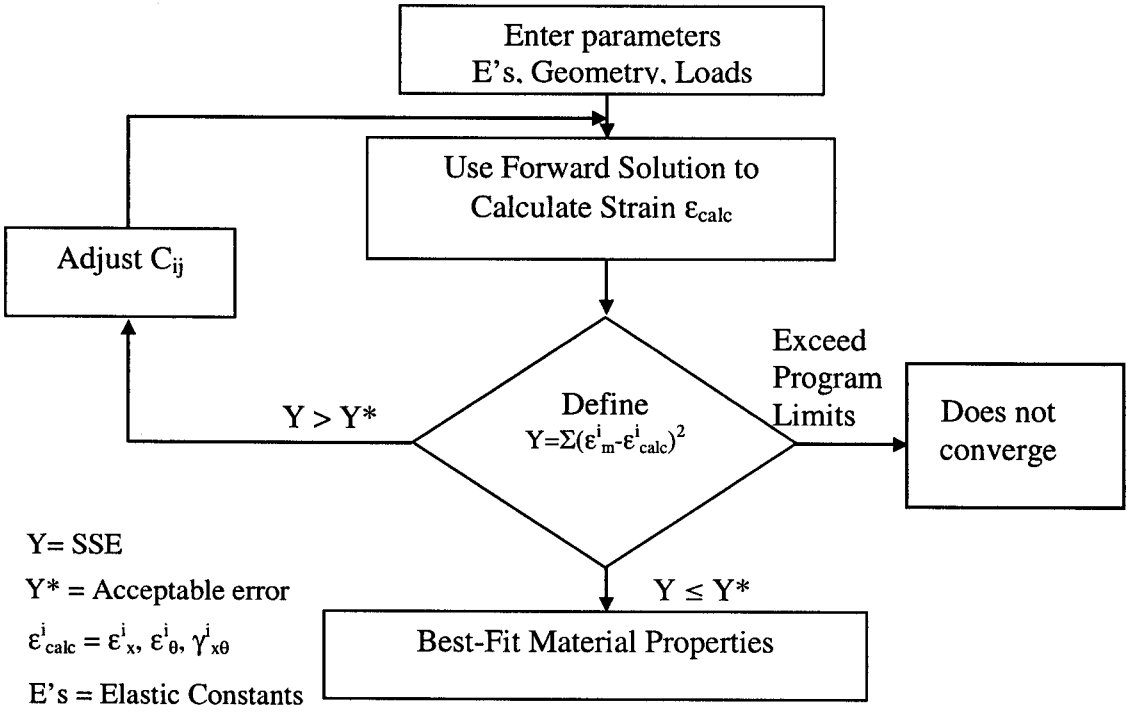

Figure 3-1: Schematic of Inversion Program

At this point, C++ codes have been written for the Forward and Inverse solutions. In order to test the method, a fictitious composite laminate data set was created, and the Forward solution was used to generate the strain response. The guess values were altered and input into the Inverse solution. Table V contains the guess values, solution values and the correct values for the test run. The maximum number of iterations was set to 25, with no other criteria used, to obtain a plot of the variation in the SSE with each iteration, as seen in Figure 3-2. After each iteration, the values are improved and the sum of squared error decreases until the solution is found (the line plateaus). The different lines are for the number of significant digits included in the strain values used as the experimental data set. Truncating the strain values before they were input into the analysis controlled the number of significant digits, illustrating the effects of error on the input values. The effect is not significant for exact values (4 or more significant digits), but does introduce large errors in some of the values in the cases of 2 or 3 significant digits. This is not unexpected, linear and nonlinear regression are very sensitive to error in the input values. This sensitivity is not desirable since the accuracy of experimental measurement can not be expected to be accurate to 4 significant digits.

Table V. Data set used in the Inversion Program (Input and Output are for 6 significant digits).

Value	Input Value	Output Value	Correct Value
E_1	10000	2.15E+07	2.15E+07
E_2	1000	1.46E+06	1.46E+06
E_3	1500	1.46E+06	1.46E+06
G_{12}	5000	5.61E+06	5.61E+06
ν_{12}	0.1	0.3	0.3
ν_{13}	0.159	0.5896	0.59
ν_{23}	0.1	0.59	0.59

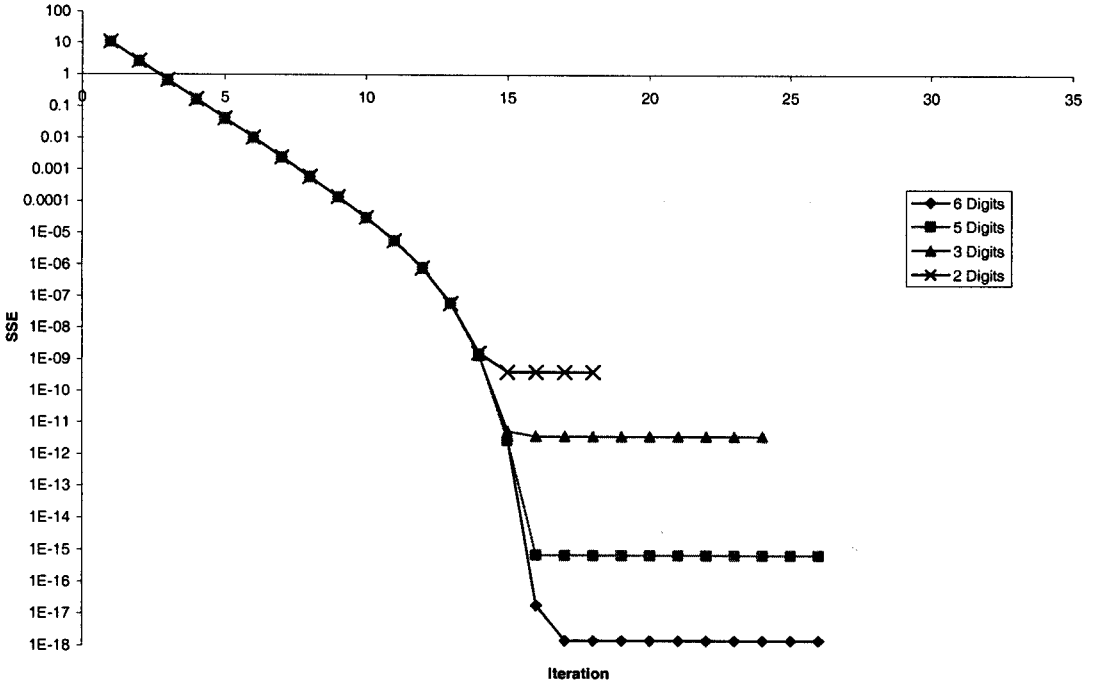

Figure 3-2: Sum of Square Error values for each iteration

Application of this method to the results reported in this paper is forthcoming. In order to accurately describe these materials, the model has been improved to include two new conditions. The first would allow for the model to describe a non-homogenous or hybrid structure. This would allow for the SiC layer in the samples to be included. The second condition is a set of degenerate solutions to the problem. After inspecting the

terms of the equations for the displacements (and the other terms, since they are functions of the displacements), both Γ, Ω,and Ψ have conditions where the denominator can equal zero (when $\bar{C}_{22} = \bar{C}_{33}$ and/or $\bar{C}_{22} = 4\bar{C}_{33}$). The first condition is not uncommon and is met with isotropic or transversely isotropic layers (0° plies). Both of these conditions are being included so that the SiC layer can be included (utilizing both additions – hybrid structure with an isotropic SiC layer). Once the work is completed, the data will be input into the analysis, and the calculation of the ply-level properties will be attempted.

4. Effect of Randomly Distributed Fibers on the Toughness of Fibril-Reinforced Composite Materials

4.1 Introduction

The critical stress for extension of short (non-steady-state) matrix cracks bridged by continuous fibers parallel to the applied load and perpendicular to the crack has been thoroughly analyzed using fracture mechanics principles by Marshall et al.[14], McCartney[15], Majumdar et al.[16]. In their analysis, authors proceed by equating the effective stress intensity factor obtained for the matrix crack, i.e., the stress intensity factor obtained by superposing the contributions of the far field stress and of the crack bridging fiber tractions with an effective fracture toughness of composite. The computation involves three key steps:

1. Development of a relation between traction applied by the crack-bridging fibers and the crack-opening displacement;
2. Use the force displacement relation in an iterative numerical scheme to obtain a self-consistent crack opening profile and crack-bridging tractions at a given applied stress;
3. Use of the self-consistent fiber tractions to calculate the effective stress intensity factor and the critical stress based on an appropriate fracture criterion.

In this work, we extend the Marshall et al.[14] approach to the analysis of inclined and randomly distributed fibers within a composite specimen.

4.2 Crack Closure Pressure for an Inclined Fiber

The mechanics of fiber pullout can be conveniently analyzed by applying tractions T_m and T_f equal and opposite to the stresses in the matrix and fibers along AA' at the end of the slipped region (as shown in Figure 4-1), and removing the section AA'CC'. If we neglect the effect of shear stresses above AA' (i.e., assume that it represents an isostrain plan) these tractions are related:

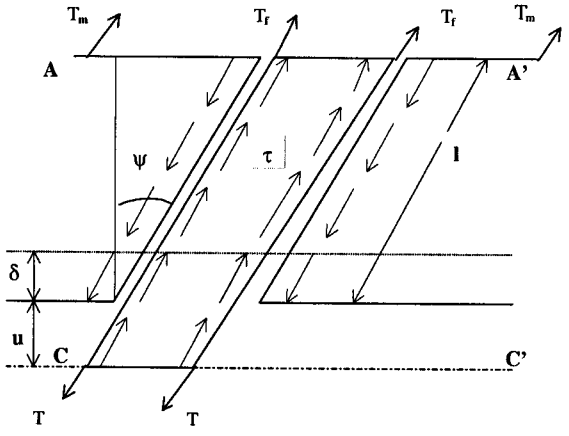

Figure 4-1: Analysis of fiber pullout for an inclined fiber

$$\frac{T_m}{E_m} = \frac{T_f}{E_f} \tag{4.1}$$

where,

T_m and T_f are the tractions within the matrix and the fiber respectively;
E_m and E_f are the modulus within the matrix and the fiber respectively.

Equations relating the stresses and displacements are obtained by considering the equilibrium of the matrix and fiber separately and also calculating the extensions δ and δ+u of the matrix and fiber Marshall et al.[14].

Matrix equilibrium:

$$T_m A_m \cos\psi = 2\pi R\tau \cos\psi \tag{4.2}$$

Fiber equilibrium:

$$T\, A_f \cos\psi = T_f\, A_f \cos\psi + 2\pi R\tau \cos\psi \tag{4.3}$$

Matrix elongation:

$$\frac{\delta}{l\,\cos\psi} = \frac{\pi R l \tau}{A_m E_m} \tag{4.4}$$

Fiber elongation:

$$\frac{\delta}{l\cos\psi} + \frac{u}{l\cos\psi} = \frac{T_f}{E_f} + \frac{\pi R l \tau}{A_m E_m} \tag{4.5}$$

where,

ψ = *fiber angle*
A_m = *area of matrix per fiber*
A_f = *fiber cross-sectional area* $A_f = \pi R^2$
R = *fiber radius*
l = *sliding length*
τ = *shear stress*
δ = *elongation*
u = *crack opening*

From Equations (4.1) and (4.2), we have

$$T_f = \frac{2\pi R l \tau}{A_m} \frac{E_f}{E_m} \tag{4.6}$$

From Equations (4.3) and (4.6), we have

$$T = \frac{2\, l\tau}{R}[1+\eta] \tag{4.7}$$

with

(4.8)

$$\eta = \frac{E_f A_f}{E_m A_m} = \frac{E_f V_f}{E_m V_m} \tag{4.9}$$

If we substitute Equations (4.4) and (4.6) into Equation (4.5) we find:

$$\frac{u}{l} = \frac{2\pi R l \tau \cos\psi}{A_m E_m} + \frac{\pi R l \tau \cos\psi}{A_f E_f} - \frac{\pi R l \tau \cos\psi}{A_m E_m} \tag{4.10}$$

After some simplification, we can find the sliding length l:

$$l^2 = \frac{u R E_f}{\tau(1+\eta)\cos\psi} \tag{4.11}$$

Finally, by combining Equations (4.7) and (4.11) we obtain the traction T:

$$T = \left[\frac{4 u E_f \tau(1+\eta)}{R\cos\psi}\right]^{1/2} \tag{4.12}$$

4.3 Extension to Randomly Distributed Fibers

4.3.1 No Possible Fiber Pull-Out

We now seek to extend the solution for the closure traction to the analysis of cracks that are bridged by randomly oriented fibers. These fibers are assumed to be sufficiently long that pullout does not occur. For such a case, the probability density function describing the orientation of fibers in the matrix is defined as (with the normalization condition)

$$\begin{aligned} F(\psi) &= \int_0^{\psi} f(\psi)\, d\psi \\ F\left(\frac{\pi}{2}\right) &= 1 \end{aligned} \tag{4.13}$$

If we consider $f(\psi)$ = constant (so that the distribution is completely random), we find that:

$$f(\psi) = \frac{2}{\pi} \tag{4.14}$$

Following Jain and Wetherhold[17], we introduce the auxiliary variable y′, which represents the signed distance from fibers' center of gravity to the crack plane. The required probability density is:

$$P[E_1 E_2] \tag{4.15}$$

where

$$\begin{aligned} E_1 &= y' \in [y', y' + d\,y'] \\ E_2 &= \psi \in [\psi, \psi + d\psi] \end{aligned}$$

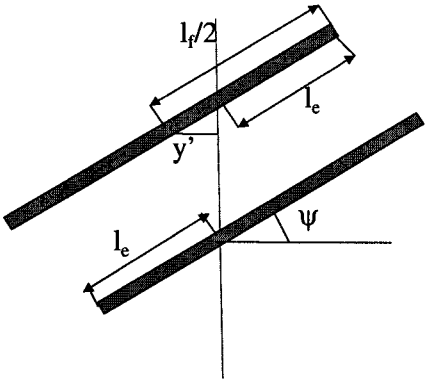

Figure 4-2: Illustration of the definition of the auxiliary variable y'

Using the Bayes' theorem for non-independent events E_1 and E_2 we can write:

$$P[E_1 E_2] = P\left[E_1 / E_2\right] P[E_2] \tag{4.16}$$

The second probability is well defined by Equation (4.14). For the events E_1 the only values of y' of interest are those which intercept the crack, i.e. $y' \in \left[\frac{-l_f}{2}\cos\psi, \frac{l_f}{2}\cos\psi\right]$. Under the assumption that the fiber center of gravity is uniformly distributed in y direction $\left[f_y(y) = \frac{1}{h}, y \in [0, h]\right]$, we can say that y' is also uniformly distributed $\left[f_{y'}(y) = \frac{1}{h}, y' \in [\Pi\text{-}h, \Pi]\right]$. We may study $y' \in \left[0, \frac{l_f}{2}\cos\psi\right]$ and multiply that probability by 2.

The probability density that a single fiber bridges an arbitrary crack plane $y' = \Pi$ with events E_1 and E_2 is thus:

$$dN_f = \begin{cases} \left(\frac{2}{\pi}\right)\left(\frac{2}{h}\right) d\psi dy' \\ 0 \ \textit{elsewhere} \end{cases} \tag{4.17}$$

The number of fibers crossing the crack plane with events E_1 and E_2 is defined as:

$$N_{fc} = \left(\frac{2}{\pi}\right)\left(\frac{2}{h}\right) N_f \int_0^{\frac{\pi}{2}} \int_0^{\frac{l_f}{2}\cos\psi} d\psi dy' \tag{4.18}$$

where,

h = *width of the composite plate*
N_f = *total number of fiber in the sample.*

$$N_f = \frac{A_c h V_f}{A_f l_f} \tag{4.19}$$

The closure pressure is defined as:

$$P(y) = T(y) V_{fc} \cos^2 \psi \tag{4.20}$$

where,

$V_{fc} = \frac{A_f l_f}{A_c h} N_{fc}$ - Volume fraction of the fibers that bridge the crack plane Π with events E_1 and E_2.

By taking into account Equation (4.18) and Equation (4.19) we can write:

$$V_{fc} = \left(\frac{2}{\pi} \frac{2}{h} \int_0^{\frac{\pi}{2}} \int_0^{\frac{l_f}{2}\cos\psi} d\psi dy' \right) V_f \tag{4.21}$$

Thus, if the crack is large enough that bridging fibers are randomly distributed, the approximate closure pressure as a function of position is given by

$$P(y) = A \int_0^{\frac{\pi}{2}} \int_0^{\frac{l_f}{2}\cos\psi} T(y) \cos^2 \psi dy' d\psi \tag{4.22}$$

where

$$\begin{aligned} A &= \left(\frac{2}{\pi} \right) \left(\frac{2}{h} \right) V_f \\ T(y) &= \left[\frac{4u(y) E_f \tau (1+\eta)}{R \cos\psi} \right]^{1/2} \end{aligned} \tag{4.23}$$

After integration we have

$$P(y) = BT'(y) \int_0^{\frac{\pi}{2}} \left(\sqrt{\cos\psi} \right)^5 d\psi \tag{4.24}$$

where

$$\begin{aligned} B &= \left(\frac{2}{\pi} \right) \left(\frac{l_f}{h} \right) V_f \\ T'(y) &= \left[\frac{4u(y) E_f \tau (1+\eta)}{R} \right]^{1/2} \end{aligned} \tag{4.25}$$

If we evaluate the integrand numerically, we obtain the final result

$$P(y) \approx 0.457 \left(\frac{l_f}{h} \right) \left[\frac{4u(y) E_f t (1+\eta)}{R} \right] V_f \tag{4.26}$$

So that for the case in which the length of the fibers is the same as the width of the composite, the average bridging stress is roughly half that which would be expected if the fibers were aligned with the loading direction.

4.3.2 Possible Fiber Pull-Out

Using the geometric relationship shown in Figure 4-2, $y' = \left(\frac{l_f}{2} - l_e\right)\cos\psi$, where l_e represents the embedded length. For the embedded length l_e defined as:

$$l_e = \frac{l_f}{2} - \frac{y\phi}{\cos y} \tag{4.27}$$

We have the following conditions:

$$\begin{cases} \text{if } l_e \geq l \quad p = p(y) \\ \text{if } l_e < l \quad p = 0 \end{cases} \tag{4.28}$$

Taking into account these conditions in Equation (4.21), changing the inner boundary limit of integration to $\left(\frac{l_f}{2} - l\right)\cos\psi$ and integrating on l rather than y' the expression of the crack closure pressure with possible pullout is:

$$P(y) \approx 0.457 \left[\frac{l_f}{h} - l\right] \frac{4u(y)E_f t(1+\nu)}{R} V_f \tag{4.29}$$

where l is the sliding length defined by Equation (4.11).

Once the crack closure pressure is obtained, it is possible to determine the crack shape and the stress intensity factor at the crack tip as a function of the global applied load.

4.4 Crack Opening and Stress Intensity Factor

The crack-opening displacement, u(Y), at any position is determined by the entire distribution of surface traction [18]:

$$u(Y) = C\int_Y^1 \frac{s}{\left(s^2 - Y^2\right)^{1/2}} \int_0^s \frac{\sigma_\infty - P(t)}{\left(s^2 - t^3\right)^{1/2}} dt ds \tag{4.30}$$

where

$$C = \frac{4\left(1-\nu^2\right)c}{\pi E_c} \tag{4.31}$$

ν = *Poisson's coefficient*
c = *half crack length*
E_c = *composite module*
Y = *normalized position coordinate, y/c*
σ_∞ = *far field stress*
P = *crack closure pressure*

By superposing the contribution of the far field and the crack closure pressure, we obtain the expression of the stress intensity factor as follows [18]:

$$K = 2\sqrt{\frac{c}{\pi}} \int_0^1 \frac{s_\infty - P(Y)}{(1 - Y^2)^{1/2}} dY \tag{4.32}$$

It is essential to ensure that the crack-opening displacement and the crack closure pressure are self-consistent with each other before any computation of the stress intensity factor. This can be achieved using numerical techniques. In this paper we used the same numerical procedure as Marshall et al.[14].

4.5 Numerical Procedure

Equation (4.30) is solved numerically using an iterative procedure. The value of the crack opening is used to compute the corresponding crack closure pressure, which will give the value of the crack opening for the next iteration. The value of u(Y) was computing at $Y = \sin\left(\frac{i*\pi}{2*n}\right)$, where i varies from 1 to n and n is the number of interval in y. We consider that the convergence to self-consistency achieved as follows:

> *If the value of the crack opening, u_n, used at iteration n to compute led to the value, u'_n, then the value to be tried at the iteration (n+1) was $\alpha u_n + (1-\alpha)u'_n$ where the damping coefficient α is set to 0.5 for short cracks and higher for larger cracks. This process was continued till the difference between the values of two successive iterations is less than a tolerance fixed by the user.*

Figure 4-3 and 4 show examples where the crack opening u and the crack closure pressure P are compared with those when the fibers are straight.

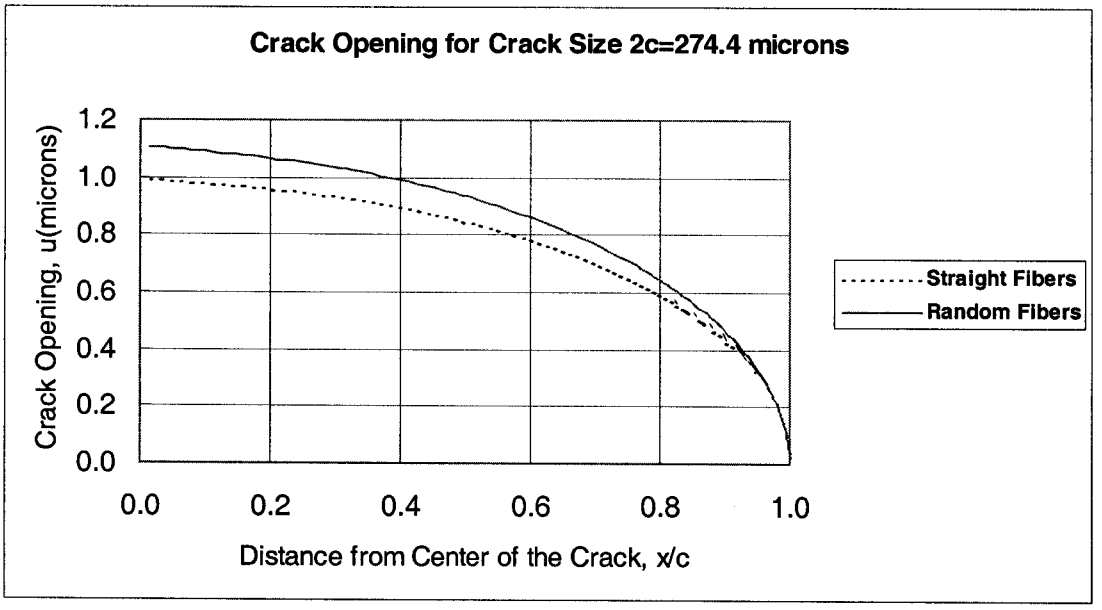

Figure 4-3. Crack opening displacement for composites reinforced with aligned fibers and randomly oriented fibers.

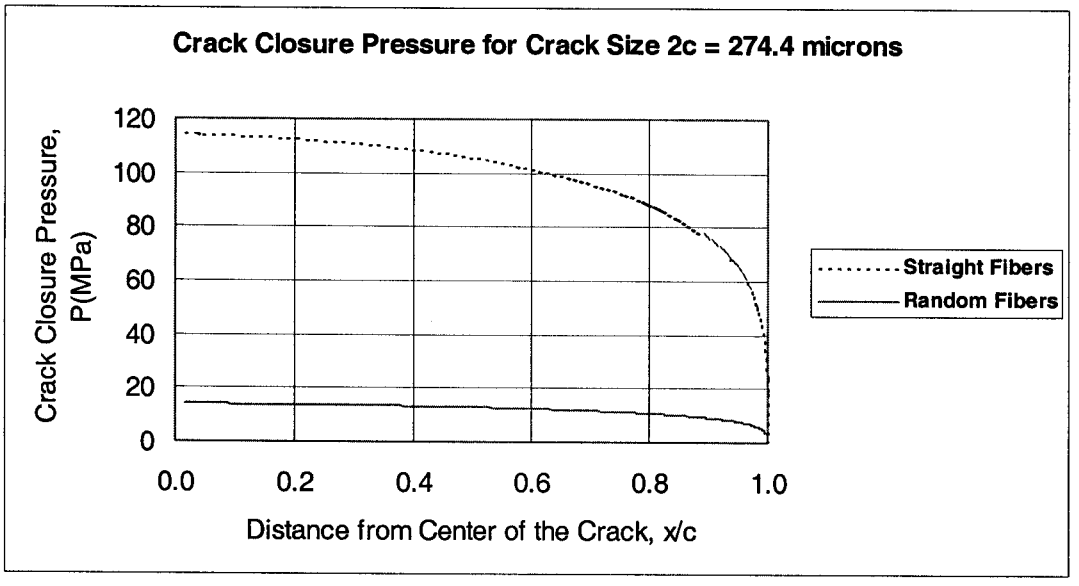

Figure 4-4. Crack closure pressure for composites reinforced with aligned fibers and randomly oriented fibers.

The sample dimension and the matrix and fiber properties used in the analysis are summarized in Table 6 and Table 7.

Table 6: Dimensions Used in Analysis

Length (cm)	Width (cm)	Thickness (cm)
15	2.5	0.25

Table 7: Summary of Fiber and Composite Properties

Property	Fiber	Matrix
$E(MPa)$	428	222
ν	0.2	0.24
$R(\mu m)$	72	
Volume Fraction	0.21	0.79
$K_c\left(MPa*\sqrt{m}\right)$	N/A	2.7

Finally, we examined the effect of fiber length in the case of possible fiber pullout. As we expected the longer the fiber is the bigger the closure pressure is. These results are represented in Figure 6 for three different lengths.

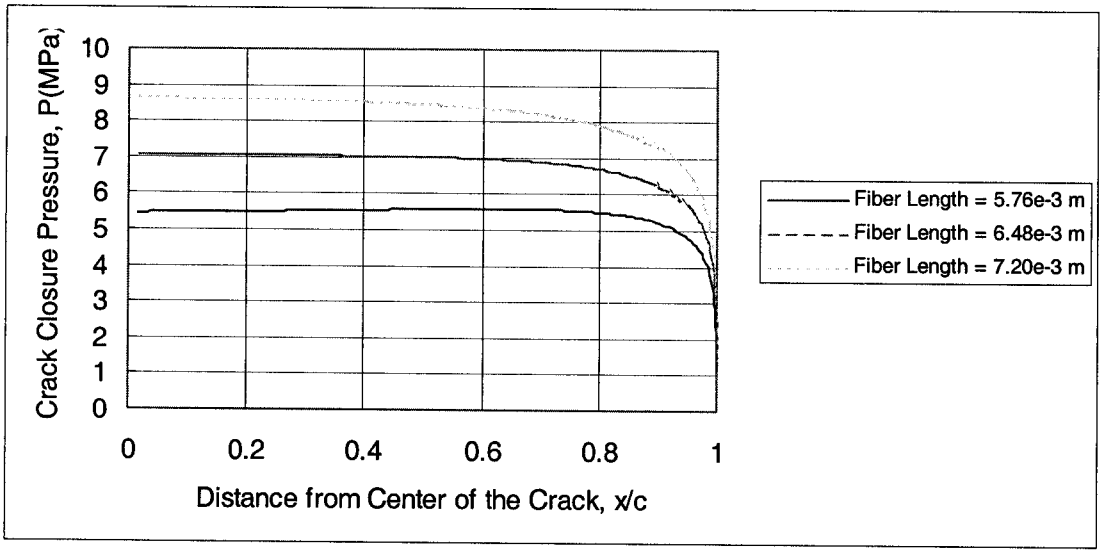

Figure 4-5. Crack closure pressure for composites containing randomly oriented short fibers as a function of fiber length.

The results of the analysis can also be used to determine the apparent toughness of the composite as a function of crack size. Such a result is shown in Figure 4-6.

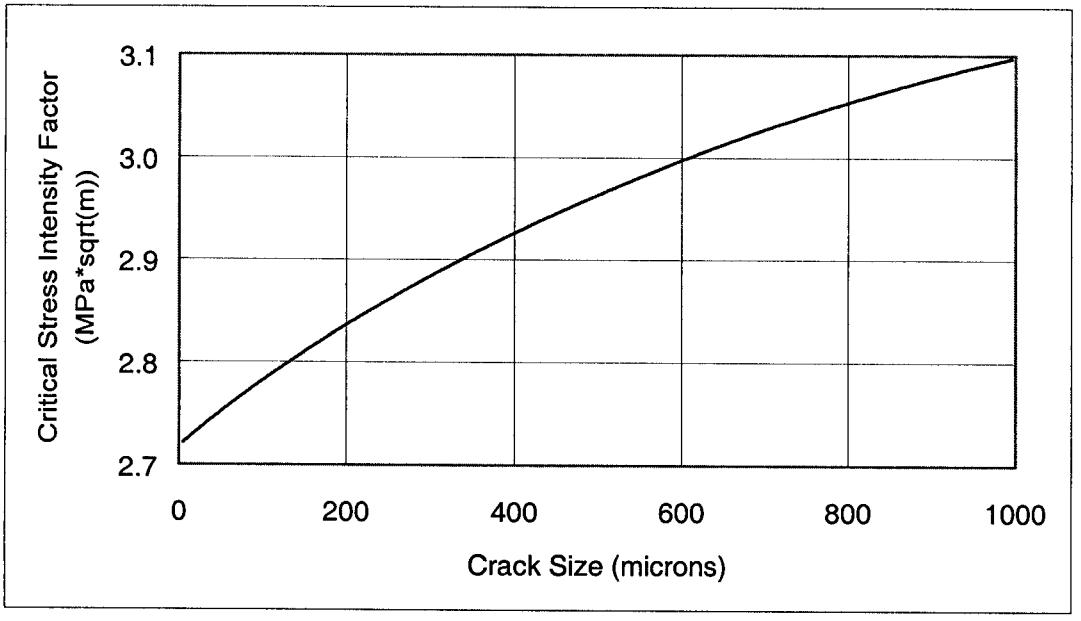

Figure 4-6. Critical stress intensity factor as a function of crack size.

5. References

1. X. Huang, R. H. Carter, and K. L. Reifsnider, "Experimental Study and Modeling of a Novel Ceramic Composite Hot Gas Candle Filter Material," *Ceramic Engineering and Science Proceedings*, **19** [3], (1998).

2. T. Besmann, B. W. Sheldon, R. A Lowden, and D. P. Stinton, "Vapor-Phase Fabrication and Properties of Continous-Filament Ceramic Composites," *Science*, 253, pp 1104-1109,1991.

3. K. R. Vaidyanathan, J. Sankar, A. D. Kelkar and B. Weaver," Mechanical Properties of Nextel 312 Fiber-Reinforced SiC Matrix Composites in Tension," *Ceramic Engineering and Science Proceedings*, 15[4], pp. 251-261, 1994.

4. K. R. Vaidyanathan, J. Sankar, A. D. Kelkar and J. Narayan, "Investigation of Mechanical Properties of Chemically Vapor Infiltrated (CVI) Ceramic Matrix Composites," *Ceramic Engineering and Science Proceedings*, 15[4], pp. 281-291, 1994.

5. K. R. Vaidyanathan, J. Sankar, A. D. Kelkar, D. P. Stinton and M. H. Headinger, "Investigation of Mechanical Properties of Chemically Vapor Infiltrated Ceramic Matrix Composites Under Pure Tension, " *Ceramic Engineering and Science Proceedings*, 14[9-10], pp. 1016-1027, 1993.

6. B. L. Weaver, R. A. Lowden, J. C. Laughlin, D. P. Stinton, T. M. Besmann and O. J. Schwarz, "Nextel/SiC Composites Fabricated Using Forced Chemical Vapor Infiltration," *Ceramic Engineering and Science Proceedings*, 14[9-10], pp. 1008-1015, 1993.

7. J. P. Singh, M. Sutaria, and W. Bielke, "Thermal Shock Behavior of Advanced Ceramic/Composite Hot-Gas Filters" *Ceramic Engineering and Science Proceedings*, **18**[3], pp.719-727, 1997.

8. R. H. Carter, X. Huang, and K. L. Reifsnider, "Experimental Study of a Ceramic Hot Gas Candle Filter,"*Ceramic Engineering and Science Proceedings*, **20** [3], pp. 153-160, 1999.

9. L. Chuck and G. Graves, "Hoop Tensile Strength and Fracture Behavior of Continuous Fiber Ceramic Composite (CFCC) Tubes from Ambient to Elevated Temperatures," *Journal of Composites Technology & Research*, Vol. 19, No. 3, pp. 184-190, 1997.

10. S. P. Timoshenko and J. N. Goodier, Theory of Elasticity, McGraw-Hill, Inc., New York, NY, pp. 68-69, 1970.

11. N. E. Dowling, Mechanical Behavior of Materials, Prentice-Hall, Inc., Englewood Cliffs, NJ, pp. 162-164, 1993.

12. Rousseau, C., M. Hyer, and S. Tompkins, "Stresses and Deformations in Angle-Ply Composite Tubes," Center for Composite Materials and Structures report #CCMS-87-04, Virginia Tech, Blacksburg, VA, 1987.

13. George, E. Master's Thesis: " A Method for the Ply-Level elastic Characterization of Composite Materials Using Thick Tubular Angle-Ply Specimens," Virginia Tech, Blacksburg, VA, 1993.

14. D. B. Marshall, B. N. Cox, A. G. Evans, "The Mechanics of Matrix Cracking in Brittle-Matrix Fiber Composites," *Acta Metall.*, **33**[11], pp. 2013-2021, 1985.

15. L. N. McCartney, "Mechanics of Matrix Cracking in Brittle- Matrix Fiber Reinforced Composites," *Proc. R. Soc. London*, A. **409**, pp. 329-350, 1987.

16. B. S. Mujumdar, G. M. Newaz, and M. D. Thouless, "Yielding Behavior of Ceramic Matrix Composites"; *Advances in Fracture Research, Proceedings of 7th International Conference on Fracture (ICF7)*, Edited by K. Salama, K. Ravi Chandar, D. M. R. Taplin, and P. Rama Rao, Pergamon Press, Oxford, UK, pp. 2805-2814, 1989.

17. L.K. Jain, R.C. Wetherhold, "The Effect of Fiber Orientation on the Fracture Toughness of Brittle Matrix Composites", *Acta. Metall. Mater*, **40** [6], pp. 1135-1143, 1992.

18. I. N. Sneddon and M. Lowengrub, "Crack Problems in the Classical Theory of Elasticity", pp. 25-28, Wiley, New York, 1969.